IOP PUBLISHING JOURNAL OF MICROMECHANICS AND MICROENGINEERING

J. Micromech. Microeng. **19** (2009) 094007 (7pp) doi:10.1088/0960-1317/19/9/094007

# A rotary microactuator supported on encapsulated microball bearings using an electro-pneumatic thrust balance

**Matthew McCarthy[1], C Mike Waits[2], Mustafa I Beyaz[3] and Reza Ghodssi[3,4]**

[1] Mechanical Engineering Department, Massachusetts Institute of Technology, Cambridge, MA 02139, USA

[2] US Army Research Laboratory, Adelphi, MD 20783, USA

[3] MEMS Sensors and Actuators Laboratory, Department of Electrical and Computer Engineering, Institute for Systems Research, University of Maryland, College Park, MD 20742, USA

E-mail: ghodssi@umd.edu

Received 13 January 2009, in final form 31 March 2009
Published 26 August 2009
Online at stacks.iop.org/JMM/19/094007

**Abstract**

The development of a rotary microactuator supported on encapsulated microball bearings and driven by electro-pneumatic actuation is reported. The encapsulated bearing provides full support to an encased rotor, while an electro-pneumatic thrust balance is used to minimize rotor normal load. By minimizing normal load, bearing friction is reduced leading to increased speed and performance. Experimental results show that the microactuator is capable of repeatable operation and continuous 360° motion at speeds of 5–2000 rpm. This is the first demonstration of a ball bearing supported electrostatic microactuator with a fully encased rotor, capable of direct mechanical attachment or reliable interaction with external media.

(Some figures in this article are in colour only in the electronic version)

## 1. Introduction

MEMS fabrication techniques have been used to create microactuators of various sizes, speeds and ranges. Most research has been focused on short-range (tens of $\mu$m) linear actuators capable of high speed (hundreds of m s$^{-1}$) and accuracy [1, 2], as well as millimeter-range linear actuators typically demonstrated at lower speeds (hundreds of $\mu$m s$^{-1}$) [3]. Rotary and angular actuators have also been realized using various actuation mechanisms including electrostatic comb-drives [4] as well as thermal actuation [5]. Due to the tethered nature of their support mechanisms, these devices are restricted to small angular motions precluding their use in applications requiring continuous rotary motion. Untethered rotary support mechanisms have been developed for MEMS applications using both direct contact bearings and more complicated gas-lubricated systems. Surface-micromachined variable-capacitance motors using sliding-mode bearings have been demonstrated [6], but these devices suffer from large friction and wear. Additionally, high-speed air bearings have been demonstrated in micromotors (55 000 rpm) and micro-turbomachinery (2 million rpm) [7, 8]. While these systems have superior speed and friction characteristics, they cannot be used in positioning systems due to the nature of the levitating rotor element and its inability to support mechanical attachments. Rotary microactuators capable of continuous motion require a robust bearing mechanism able to provide low-friction support over a range of operating conditions and allow for useful attachment and/or interaction with external media.

Our group has pioneered the development of microfabricated ball bearings and their use as support mechanisms for rotary MEMS devices [9–16]. Ghalichechian *et al* demonstrated the first rotary microactuator supported on MEMS-fabricated ball bearings using variable-capacitance actuation of a silicon disk [11]. While the microballs allow for continuous rotary motion and stable operation, a key disadvantage of this device was the unrestrained nature

[4] Author to whom any correspondence should be addressed.

 © 2009 IOP Publishing Ltd Printed in the UK

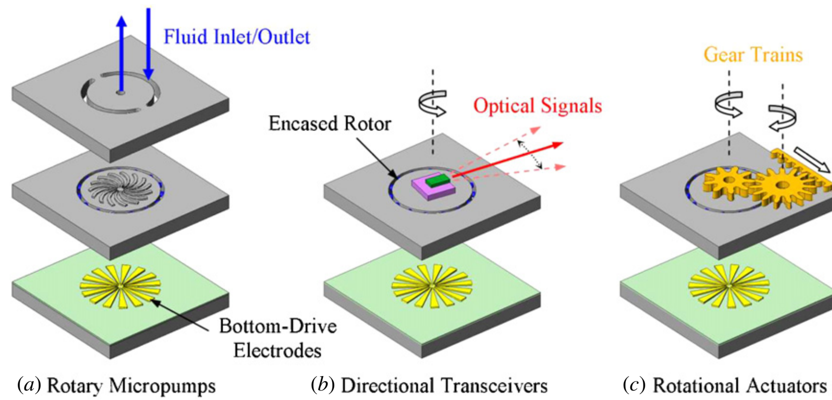


**Figure 1.** Application examples of bottom-drive variable-capacitance microactuators: (*a*) rotary micropumps, (*b*) directional transceivers and (*c*) rotational actuator systems.

of the rotor. The rotating element simply rested on the microballs and is held in place with electrostatic forces. Useful implementation of a microball bearing supported actuator will require direct mechanical attachment and/or interaction with the rotor. Accordingly, encapsulated microball bearings were developed using a notably more complicated fabrication process initially demonstrated in micro-turbomachinery [12–16]. In this design, the rotor is fully supported by microballs around its entire periphery. Using microturbine actuation, the encapsulated microball bearings have been actuated at speeds of up to 50 000 rpm and tribologically characterized through spin-down testing [16]. Previous publications on the development [12, 13] and characterization [14–16] of encapsulated microball bearings have shown the importance of minimizing the thrust load supported by the microballs. Empirical modeling of bearing friction has shown a strong relationship between bearing friction and normal load [16]. In addition, smooth repeatable rotation was observed for small loads while large wear and deterioration in performance was seen at higher loads.

Accordingly, this work presents the development of a novel bottom-drive electrostatic microactuator supported on encapsulated microball bearings using a pneumatic thrust balance to reduce normal load, therefore increasing speed and performance. The rotor is fully supported using an encapsulated bearing design, allowing this device to be implemented for a variety of microsystems applications. Figure 1 shows schematic representations of several applications for such devices, leveraging the structural integrity of an encased rotor and an increased active area using bottom-drive variable capacitance actuation. Figure 1(*a*) shows an electrically actuated micropump based on a spiral groove viscous pumping principle, while figure 1(*b*) shows a rotary stage capable of 360° rotation for optical transceiver systems. Additionally, the fully supported rotor can be envisioned as a drive mechanism for a variety of actuator systems including gear trains as shown in figure 1(*c*). The key advantages of a MEMS-fabricated microball bearing supported actuator are the ability to integrate micro/nano-fabricated structures directly on to the rotor and the ability to scale these technologies to smaller dimensions. The silicon rotary platform provides an ideal substrate for bulk or surface

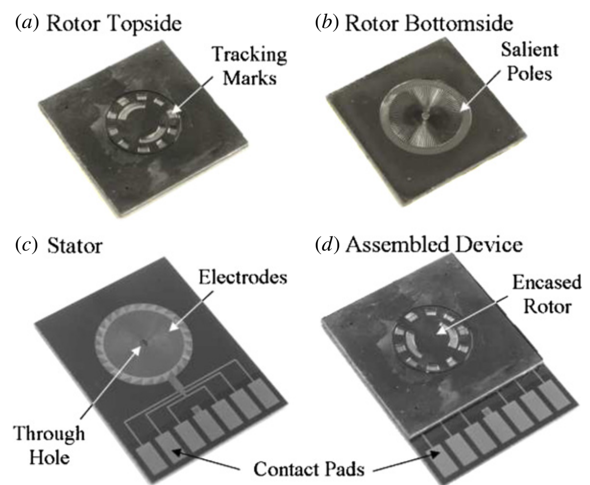


**Figure 2.** Photographs of the encased rotor: (*a*) topside showing tracking marks; (*b*) bottom side showing salient poles; (*c*) the stator with embedded electrodes and through hole; (*d*) the assembled device.

micromachined optical, inertial or mechanical transducers, leaving the underside available for actuation and control. While the development of a 10 mm diameter bottom-drive rotary actuator is presented, these technologies are envisioned for sub-millimeter scale devices. This work demonstrates a proof of concept device capable of useful mechanical attachment, continuous synchronous operation and a scalable fabrication process.

## 2. Device

Using the previously reported encapsulated microball-bearing design [16] and variable-capacitance electrode design [11] a rotary microactuator has been fabricated and characterized in this work. Figure 2 shows optical photos of the fabricated components and an assembled device, while figure 3 shows a schematic representation of the microactuator cross section and thrust balance operation. A silicon rotor ($\text{Ø} = 10$ mm) is fabricated with approximately 90 stainless steel microballs ($\text{Ø} = 285 \pm 0.25\ \mu$m) encased within the circular raceway

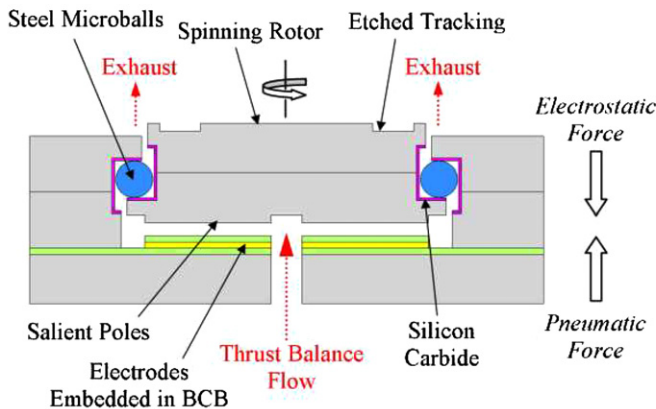


**Figure 3.** Schematic of the rotary microactuator showing electro-pneumatic thrust balance operation.

around its periphery. The rotor is made from two bonded wafers and is free to rotate about its center while being fully restrained in all other directions. Silicon carbide is conformally sputtered onto the bearing raceway surfaces to act as a friction-reducing hard coating. Tracking marks are etched into the topside of the rotor (figure 2(*a*)), while 104 salient poles are etched into the bottom side of the rotor (figure 2(*b*)). The stator consists of an array of 156 electrodes fabricated in a six-phase design and embedded in benzocyclobutene (Cyclotene 4022-35 from Dow Chemical), a low-k spin-on dielectric (figure 2(*c*)). The rotor layer sits on top of the stator (figure 2(*d*)) and is aligned using etched ball pits containing a single microball; a central through hole for thrust balance flow is etched in the stator. The rotor is lifted into contact with the microballs using pressurized nitrogen, and actuated via in-plane electrostatic forces in the form of six-phase sinusoidal signals (figure 3). The downward electrostatic force is balanced by the upward pneumatic force which is controlled externally with a high-sensitivity flow control valve. While the current devices require a pneumatic force from pressurized gas, it is unlikely that such a supply will be readily available in an integrated microsystem. This work focuses on studying the effects of thrust load on bearing friction, and therefore actuation speed, and uses pressurized nitrogen to provide a convenient counterbalance to the electrostatic normal force. Future rotary actuators will require novel replacements for this balancing force if high-speed actuation is needed. For rotary positioning applications this may not be necessary, as speeds of up to several hundred rpm have already been demonstrated without thrust balances [11]. For applications requiring continuous rotation (micromotors and micropumps) this hydrostatic balancing force can be replaced with a hydrodynamic thrust bearing to provide pressurization without external components [17].

## 3. Fabrication

The rotary microactuator consists of three wafers, and is fabricated using a series of surface and bulk micromachining techniques as shown in figures 4–6. The rotor layer fabrication (figure 4) begins with two double-side-polished 4 inch silicon

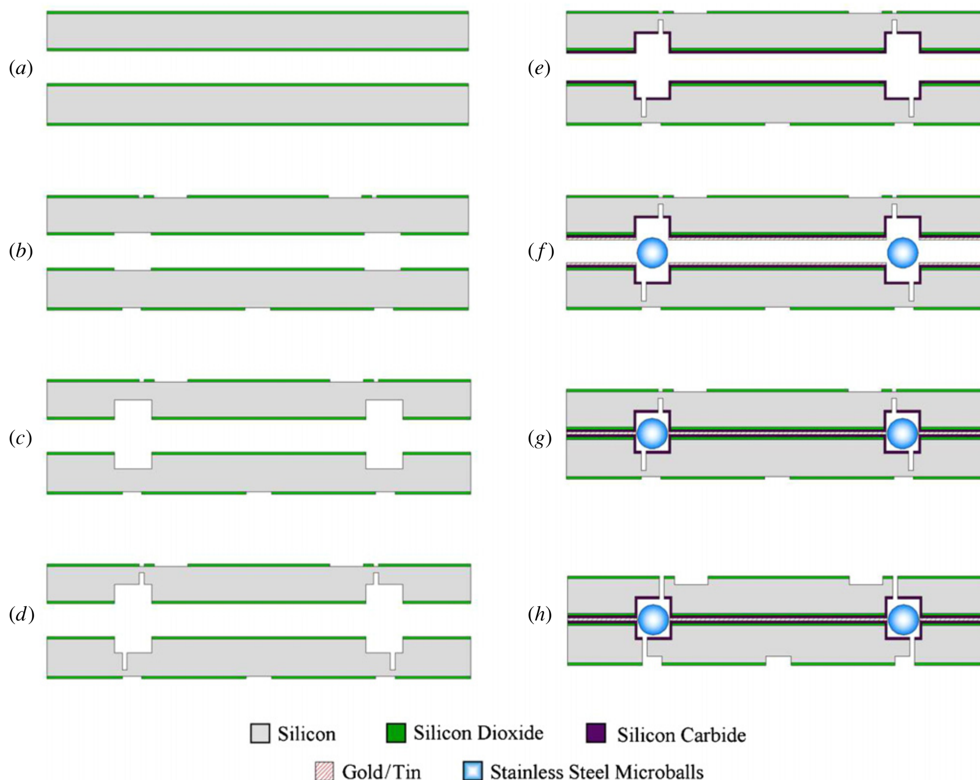


**Figure 4.** Fabrication process flow for the rotor layer.

wafers with a total thickness variation of less than 2 $\mu$m. The low-thickness-variation wafers are necessary to maintain a uniform gap over the electrostatic drive elements while the rotor spins. Matching alignment marks are first patterned on both sides of each wafer using a backside alignment technique with a measured alignment accuracy of less than 2 $\mu$m. Thermal oxide is patterned to define hard masks for the tracking marks, salient poles and bearing housings on each side of the two wafers (figure 4(*b*)). Circular trenches are etched in both wafers using a deep reactive ion etching (DRIE) process to define the bearing housing (figure 4(*c*)). The rotor's journal gaps are etched using a spray-coated photoresist masking layer (figure 4(*d*)); these etches are used to release the rotor in the final fabrication step. The journal gaps are 30 $\mu$m wide and approximately 150 $\mu$m deep while the ball housings are 290 $\mu$m wide and 290 $\mu$m deep. One micrometer of sputtered silicon carbide is conformally coated on both wafers, filling the bearing housing to act as a friction-reducing hard film (figure 4(*e*)). A gold/tin bonding layer (50 nm Cr, 50 nm Au, 1 $\mu$m AuSn, 50 nm Au) is evaporated through a shadow mask on both wafers and approximately 90 stainless steel microballs are placed in each bearing housing (figure 4(*f*)), filling roughly 85% of the raceway. The wafers are then eutectically bonded at 330 °C in a $H_2N_2$ environment under an applied load (figure 4(*g*)). The estimated alignment accuracy of the bonded rotor layers was $\pm 2$ $\mu$m. Finally, the rotor is released by etching through the previously patterned hard masks to define the rotor periphery, tracking marks on the topside and salient poles on the bottom side (figure 4(*h*)). Additionally, this step etches ball pits for rotor-to-stator alignment that are not shown in the figure.

Figure 5 shows the stator layer fabrication beginning with a 4 inch silicon wafer with 1 $\mu$m of thermal oxide (figure 5(*a*)). The oxide is patterned and dry etched to define the central through hole for thrust balance flow as well as ball pits to be used for alignment (figure 5(*b*)). Gold lines for electrical connection to the various electrode phases are deposited and patterned using wet etching (figure 5(*c*)). Benzocyclobutene, a photo-definable low-k dielectric polymer, is spun to a thickness of 3 $\mu$m and patterned to define vias, isolating the electrical connections from the electrodes (figure 5(*d*)). Gold is then deposited and patterned through a lift-off process to define the stator electrodes (figure 5(*e*)). Finally, a 3 $\mu$m passivation layer of benzocyclobutene is patterned over the electrodes and the central through hole is etched along with ball pits (not shown) for alignment to the rotor layer (figure 5(*f*)).

The rotor and stator layers are diced into individual dies and assembled using a microball alignment technique, as shown in figure 6. Four etched ball pits are fabricated on the bottom side of the rotor layer and topside of the stator layer. A single microball is placed in each pit and the two layers are assembled manually. The accuracy of this alignment technique was measured to be $\pm 5$ $\mu$m, based on variations in the as-fabrication dimensions. This alignment is crucial for proper device operation and the effects of misalignment will be addressed in more detail in section 5.

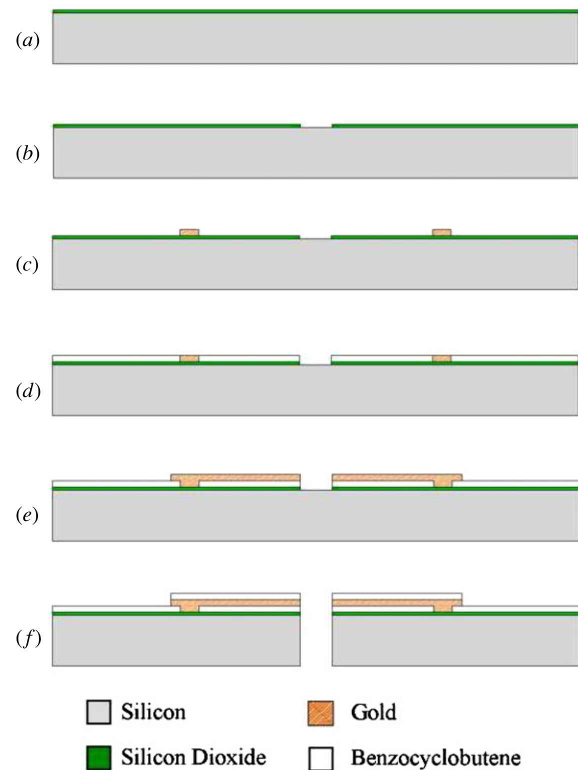


**Figure 5.** Fabrication process flow for the stator layer.

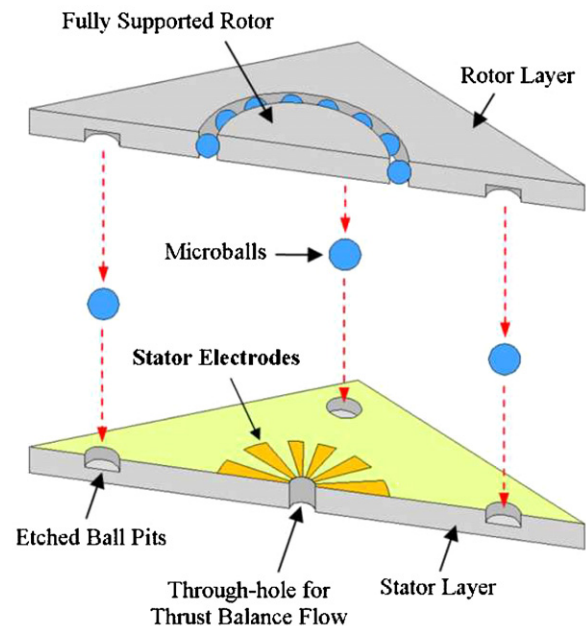


**Figure 6.** Schematic of the microball alignment technique between the rotor and stator layers.

## 4. Testing and results

A photograph of the packaged device being tested is shown in figure 7. The device is sandwiched between two plastic manifolds using o-rings for mechanical support and thrust balance flow, while the six electrode phases and a ground connection are made using an array of probes. The rotor

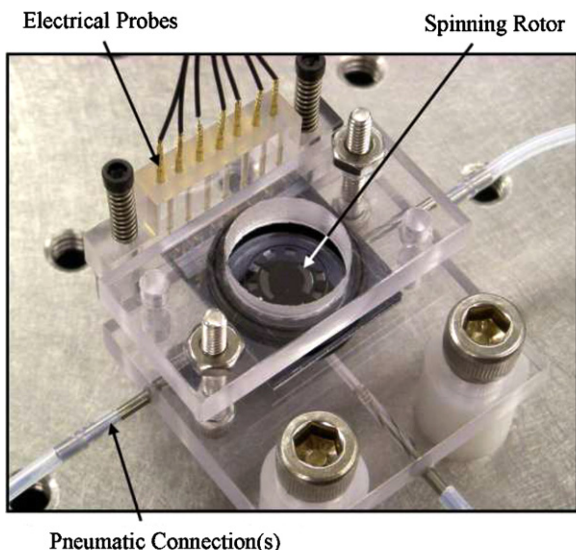


**Figure 7.** Photograph of a packaged device being tested.

is actuated using six-phase sinusoidal signals while speed is measured by monitoring the tracking marks on the rotor topside with an optical displacement sensor.

Pressurized nitrogen lifts the rotor into contact with the microballs, and the resultant upward force is balanced by a downward electrostatic force from the variable-capacitance actuation mechanism. By minimizing the net force supported by the microballs, friction and wear can be greatly reduced resulting in increased speed and performance. Figure 8 shows the maximum achieved speed plotted as a function of peak excitation voltage at various thrust pressures, where the required flow rates vary from 1 to 10 l $\min^{-1}$. For each thrust pressure the device can operate over a range of voltages. Below this range, the variable-capacitance drive mechanism cannot provide enough torque to overcome bearing friction. Above this range the electrostatic normal force is too large, the rotor is pulled downward contacting the stator and synchronization with the electrical signal is lost. For each pressure, a distinct maximum can be seen where the electrostatic and pneumatic forces balance, while still providing the minimal upward force necessary for reliable operation. This demonstrates the ability to operate at optimal normal loads using the thrust balance mechanism.

The peak operating voltage at which the rotor snaps down is plotted in figure 9 as a function of the thrust balance pressure difference. The snap-down voltage increases with thrust pressure to the one-half power; this is consistent with first-order approximations for the counteracting thrust forces. Neglecting edge effects, the electrostatic force between rotor poles and stator electrodes increases with voltage squared, while the pneumatic force increases linearly with the pressure difference. The characterization curves in figures 8 and 9 provide the optimal voltage and pressure operating conditions for stable actuation of the micromotor leading to maximum speeds.

In addition to increased speed, this device demonstrates a substantial increase in stability and reliability, showing indefinite operation at speeds as low as 5 rpm and as high as 2000 rpm for up to 2 h with no loss of synchronization. The actuator is capable of abruptly starting and stopping, as well as dynamically switching directions at speeds as high as 50 rpm. Figure 10 shows the controlled acceleration and deceleration of the rotor at an optimal loading of 150 V peak sinusoidal excitation and 4 psi of thrust pressure. The maximum demonstrated speed of 2000 rpm represents a fourfold increase as compared to previous devices using a ‘free-rotor’ design and without thrust balance capabilities [11].

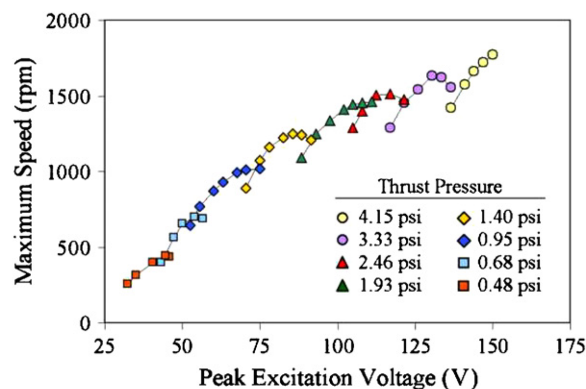


**Figure 8.** Maximum achievable speed as a function of the peak sinusoidal voltage for various thrust pressures.

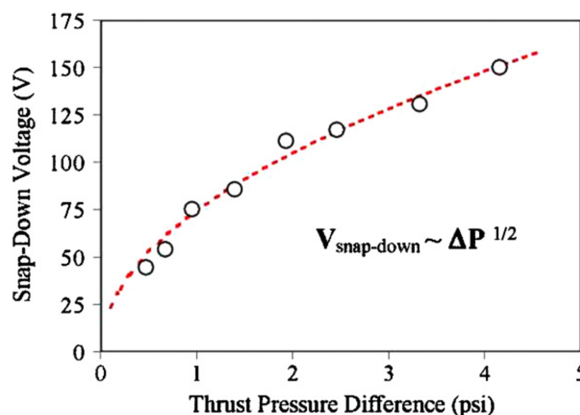


**Figure 9.** Peak sinusoidal voltage resulting in snap-down as a function of the thrust pressure difference.

## 5. Discussion

The tested device has a pole-to-electrode gap of 4.5 ± 1.5 $\mu$m varying across the rotor. This corresponds to 5.25–10.5 $\mu$N m of available electrostatic torque, as per numerical simulations of the variable-capacitance actuation mechanism reported by Ghalichechian *et al* [11]. Previous publications on the empirical modeling of bearing friction have demonstrated a friction torque constant (the ratio of friction torque to bearing speed) as low as $2 \times 10^{-4}$ $\mu$N m/rpm for encapsulated microball bearings at low normal loads [16]. Assuming that the power generated by the electrostatic drive mechanism is dissipated completely within the microball support mechanism, these two factors suggest that the

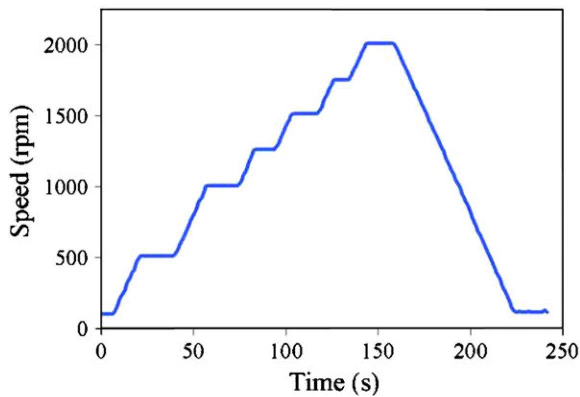


**Figure 10.** Microactuator performance, showing controlled accelerations and decelerations up to 2000 rpm at 150 V peak actuation voltage and 4 psi of pneumatic thrust pressure.

microactuator could operate at speeds as high as 26 000–52 000 rpm. While discrepancies between the as-fabricated and modeled geometry could account for moderate deviations from the predicted performance, the device's maximum operating speed is an order of magnitude lower than expected. This order-of-magnitude difference is attributed to the nature of the failure mechanism as well as misalignment in the assembled device. The failure mechanism at high speeds can be attributed not only to a lack of power available to overcome bearing friction, but also to a loss of synchronization due to perturbations from ideal rotary motion. As speed increases, random vibrations and disturbances associated with ball-to-ball as well as ball-to-housing collisions may affect the actuators ability to maintain synchronization.

Additionally, the overestimation of rotor speed is attributed to the effect of a net radial load supported by the bearing due to rotor-to-stator layer misalignment. The width of the bearing housing is 290 $\mu$m with a variation due to misalignment in the rotor layer eutectic bond of up to 2 $\mu$m, while the microball diameter is 285 $\mu$m. This creates 1.5–3.5 $\mu$m of clearance on each side of the microballs when encased in the housing. As discussed earlier, the ball pit alignment technique used to assemble the rotor and stator layers results in a measured misalignment of up to $\pm 5$ $\mu$m. Figure 11 demonstrates how this misalignment leads to a net radial load supported by the bearing. When the layers are misaligned during assembly, the stator electrodes and rotor poles are offset from one another (figure 11(*a*)). During microactuator operation, the electrostatic drive mechanism not only spins the rotor but also simultaneously attracts the poles into a state of perfect alignment with the electrodes (figure 11(*b*)). If the layers are misaligned by greater than $\pm 1.5$ $\mu$m, there is not enough play in the bearing to allow the rotor to align to the stator. This results in a net radial load in the direction opposite to the layer misalignment (figure 11(*c*)). The radial load is supported by only a few microballs on one small section of the rotor periphery, drastically changing the nature of the contact mechanics and rolling motion as well as dramatically increasing bearing friction. The previously reported results for bearing friction were measured using a turbine-actuated spin-down technique [16]. In that work, the

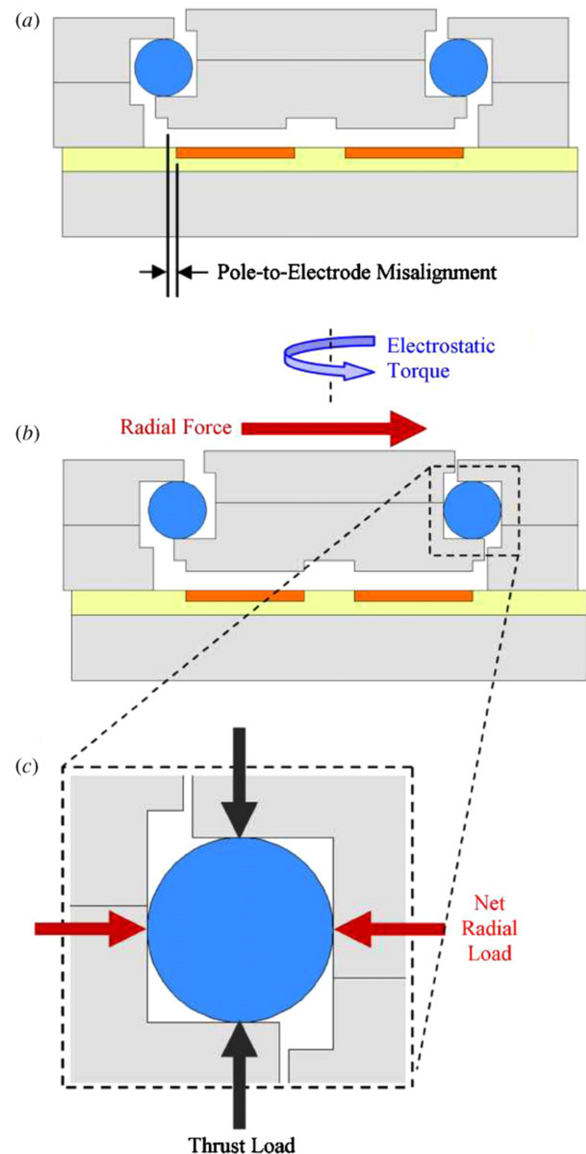


**Figure 11.** Schematic of the misaligned assembly showing (*a*) the rotor-to-stator layer misalignment, leading to (*b*) an electrostatic radial force during actuation, which results in (*c*) a net radial load supported by a the microballs.

rotor is allowed to spin down under a controlled normal load but in the absence of net radial or tangential forces. The addition of a net radial force in the current device is believed to substantially increase bearing friction and explain the order-of-magnitude difference between the expected and observed performances. Future devices will more accurately account for these effects by widening the bearing housing and thus allowing the rotor to self-align to the stator electrodes without contacting the bearing housing in the radial direction.

## 6. Conclusion

This work presents the fabrication and operation of a bottom-drive variable-capacitance rotary microactuator supported on encapsulated microball bearings using an electro-pneumatic thrust balance. The thrust balance, along with a

friction-reducing silicon carbide hard coating, has been used to minimize bearing friction and increase speed and performance as compared to previous microball-bearing supported devices. The fully supported rotating element is capable of continuous motion and repeatable operation at speeds of 5–2000 rpm. The results shown here demonstrate the feasibility of microball-bearing support mechanisms for use in next-generation rotary microsystems. This is the first microball-bearing supported electrostatic actuator capable of useful attachment or interaction with external elements. This technology is being implemented in the development of optical transceiver systems as well as electrically actuated rotary micropumps.

## Acknowledgment

This work was supported by the US Army Research Laboratory under grant no CA#W911NF-05-2-0026.

## References

[1] Huang C *et al* 2002 *J. Microelectromech. Syst.* **11** 222–35
[2] Ko J S *et al* 2002 *Appl. Phys. Lett.* **81** 547–9
[3] Cusin P, Sawai T and Konishi S 2000 *J. Micromech. Microeng.* **10** 516–21
[4] Lim T S *et al* 2004 *IEEE J. Sel. Top. Quantum Electron.* **10** 558–62
[5] Heo S and Kim Y K 2007 *J. Micromech. Microeng.* **17** 2241–7
[6] Tai Y, Fan L and Muller R 1989 *Proc. IEEE Int. Conf. MEMS* pp 666–9
[7] Livermore C *et al* 2004 *J. Microelectromech. Syst.* **13** 465–71
[8] Frehette L *et al* 2005 *J. Microelectromech. Syst.* **14** 141–52
[9] Modafe A *et al* 2006 *J. Micromech. Microeng.* **16** S182–90
[10] Ghalichechian N, Modafe A, Lang J and Ghodssi R 2007 *Sensors Actuators* A **136** 416–503
[11] Ghalichechian N, Modafe A, Beyaz M I and Ghodssi R 2008 *J. Microelectromech. Syst.* **17** 632–42
[12] Waits C M, Geil B and Ghodssi R 2007 *J. Micromech. Microeng.* **17** S224–9
[13] Waits C M *et al* 2007 *14th Int. Conf. on Solid-State Sensors, and Microsystems* pp 1131–4
[14] McCarthy M, Waits C M and Ghodssi R 2007 *7th Int. Workshop on Micro and Nanotechnology for Power Generation and Energy Conversion Application* pp 241–4
[15] McCarthy M, Waits C M and Ghodssi R 2008 *Solid-State Sensor, Actuator, and Microsystems Workshop* pp 170–3
[16] McCarthy M, Waits C M and Ghodssi R 2009 *J. Microelectromech. Syst.* **18** 263–73
[17] Wong C *et al* 2004 *J. Microelectromech. Syst.* **13** 158–64